Application Note
Energy and Chemicals

Rapid Analysis of Elemental Impurities in Battery Electrolyte by ICP-OES

Quality control measurement of 12 elements in lithium hexafluorophosphate

Download now

Agilent | Trusted Answers

ADVANCED ENERGY MATERIALS
www.advenergymat.de

Aerosol Assisted Solvent Treatment: A Universal Method for Performance and Stability Enhancements in Perovskite Solar Cells

Tian Du, Sinclair R. Ratnasingham, Felix U. Kosasih, Thomas J. Macdonald, Lokeshwari Mohan, Adriana Augurio, Huda Ahli, Chieh-Ting Lin, Shengda Xu, Weidong Xu, Russell Binions, Caterina Ducati, James R. Durrant, Joe Briscoe, and Martyn A. McLachlan**

This paper is dedicated to Dr. Russell Binions, who was the academic supervisor for Sinclair and Lokeshwari. They were both beginning their academic and scientific journeys when tragically Russell's life was cut short. He was an incredible co-author, colleague, supervisor, and friend who is dearly missed.

Metal-halide perovskite solar cells (PSCs) have had a transformative impact on the renewable energy landscape since they were first demonstrated just over a decade ago. Outstanding improvements in performance have been demonstrated through structural, compositional, and morphological control of devices, with commercialization now being a reality. Here the authors present an aerosol assisted solvent treatment as a universal method to obtain performance and stability enhancements in PSCs, demonstrating their methodology as a convenient, scalable, and reproducible post-deposition treatment for PSCs. Their results identify improvements in crystallinity and grain size, accompanied by a narrowing in grain size distribution as the underlying physical changes that drive reductions of electronic and ionic defects. These changes lead to prolonged charge-carrier lifetimes and ultimately increased device efficiencies. The versatility of the process is demonstrated for PSCs with thick (>1 µm) active layers, large-areas (>1 cm^2) and a variety of device architectures and active layer compositions. This simple post-deposition process is widely transferable across the field of perovskites, thereby improving the future design principles of these materials to develop large-area, stable, and efficient PSCs.

1. Introduction

Metal-halide perovskite materials have had significant impact across a variety of emerging optoelectronic platforms, extending beyond their initial study in photovoltaics (PVs)[1] to creating disruption in the light emitting diode, photodetector and thin film transistor research areas.[2–4] Within the PV field, the progress of perovskite solar cell (PSC) development has been underpinned by simultaneous advances in thin-film deposition,[5,6] compositional modification,[7–9] changes to the charge selective interlayers,[10,11] interface modification,[12–14] and the incorporation of a wide variety of additives.[15–18] Many of these strategies require precise control of interlayer thickness as well as additive and/or dopant concentration.[12] The concentration of such additives/dopants are incredibly

Dr. T. Du, Dr. S. R. Ratnasingham, L. Mohan, H. Ahli, Dr. C.-T. Lin, Dr. S. Xu, Prof. M. A. McLachlan
Department of Materials and Centre for Processable Electronics
Molecular Science Research Hub
Imperial College
London W12 0BZ, UK
E-mail: martyn.mclachlan@imperial.ac.uk

The ORCID identification number(s) for the author(s) of this article can be found under https://doi.org/10.1002/aenm.202101420.

[†]Deceased 2017.

Dr. T. Du, Dr. T. J. Macdonald, Dr. C.-T. Lin, Dr. W. Xu, Prof. J. R. Durrant
Department of Chemistry and Centre for Processable Electronics
Molecular Science Research Hub
Imperial College
London W12 0BZ, UK

Dr. S. R. Ratnasingham, A. Augurio, Dr. R. Binions,[†] Dr. J. Briscoe
School of Engineering and Materials Science
and Materials Research Institute
Queen Mary University of London
London E1 4NS, UK
E-mail: j.briscoe@qmul.ac.uk

F. U. Kosasih, Prof. C. Ducati
Department of Materials Science & Metallurgy
University of Cambridge
Cambridge CB3 0FS, UK

DOI: 10.1002/aenm.202101420

low,[17,19] thus inadvertently these strategies for improvement may place significant constraints on future high volume manufacturing and almost certainly create challenges of reproducibility for lab-scale devices.

Grain boundaries (GBs), whilst unavoidable in solution-deposited PSCs, are unwanted microstructural features. They potentially host crystallographic defects, for example, vacancies, interstitials, and antisites,[20] all of which create intra-bandgap states that act as electronic traps.[21] GBs orientated normal to the substrate are also reported to be i) fast channels for ionic transport[22,23] thus contribute significantly to device hysteresis,[24] ii) pathways for oxygen ingress[25] and, iii) susceptible areas for the formation of impurity phases.[26] Whilst GBs parallel to the substrate present additional barriers to charge transport.[6] To date, numerous methods have been utilized to mediate these negative effects such as passivation of GBs through additive engineering,[27,28] directed crystal growth,[29,30] promotion of larger grain formation,[31,32] and by eliminating GBs entirely by fabricating PSCs from single crystals.[33,34] However, as noted many of these approaches are extremely challenging to transfer to large-scale processing, requiring either precise control of additive amounts or long processing times, or are applicable to only a small range of perovskite compositions or processing routes.

Here we present a novel, rapid and scalable aerosol treatment method as a technique that significantly improves the crystallinity of perovskite thin films, that is, substantially enhances grain size/reduces GB concentrations. The resulting PSCs exhibit remarkably enhanced power conversion efficiencies (PCEs), increased stabilities and considerably improved reproducibility compared with as-prepared films, and those treated using alternative methods. Importantly, we demonstrate the versatility of our technique by applying it to $CH_3NH_3PbI_3$ ($MAPbI_3$) PSCs with active layer thicknesses ranging from 500–1300 nm, to large-area (>1 cm^2) devices, and to a variety of device architectures. To fully demonstrate the universality of the treatment we also show performance improvements in $Cs_{0.1}FA_{0.9}Pb(I_{0.95}Br_{0.05})$ devices.

2. Results and Discussion

2.1. Tuning the Aerosol Treatment for Optimum Device Performance

The aerosol treatment is carried out in a cylindrical quartz reactor with substrates placed on a heated graphite block (Figure S1, Supporting Information). A solvent aerosol, in this case N,N-dimethylformamide (DMF), is created using a piezoelectric mister outside the reactor and carried into the reactor by a N_2 carrier gas. The gas/solvent mixture flows through the reactor, interacting with the substrates before passing to an exhaust. The processing parameters, that is, temperature, flow rate and treatment time can be readily controlled creating a highly controllable and reproducible process. We performed 3D computational fluid dynamics (CFD) simulations of the flow rate in the cylindrical reactor and shown in **Figure 1**a the side view and in Figure 1b the cross-sectional view of the flow rate distribution. The data show a stable laminar flow forming above the perovskite film. Critically, the laminar nature of this flow creates a static aerodynamic boundary layer with a zero flow rate between the aerosol stream and the substrate, which allows only vapor diffusion through the boundary layer whilst preventing unwanted issues such as vapor condensation. This in-turn enables a more uniform interaction of solvent with the perovskite film surface.

It is important to note that during the aerosol treatment the as-deposited films remain solid, that is, there is no dissolution and/or recrystallization of the perovskite film. The proposed mechanism for grain growth is shown schematically in Figure 1c. The aerosol containing solvent droplets is transported to the surface of perovskite film, at which the droplets vaporize to form chemical vapor. Here, the quantity of DMF vapor near the film surface is insufficient to fully dissolve the film. Instead, the vapor promotes inter-grain mass transport, and due to their high surface energy, the smaller grains are eliminated with material transferred to the larger grains promoting their growth. We show in Figure 1d–g the typical surface scanning electron microscope (SEM) images of as-deposited $MAPbI_3$ and aerosol-treated $MAPbI_3$ for 2, 5, and 10 min, and in Figure 1h the statistical data of the lateral grain size. The results indicate a continuous increase of average grain size as aerosol exposure time is increased. The 2 min films typically exhibit smaller grains co-existing with the larger grains (Figure 1e), whist the 5 min film mainly consists of larger grains (Figure 1f) accompanied with a reduction of grain size distribution (Figure 1h). This is consistent with an Ostwald ripening model,[35], that is, grain coarsening where the growth of large grains occurs by the consumption of small grains. Owing to the constant supply of aerosol, extending the treatment to 10 min leads to continuous grain growth, resulting in an undesirable morphology, including pinholes, voids (Figure 1g), and increased surface roughness (Figure S2a–c, Supporting Information). We believe this can be ascribed to the morphological transitions that occur during grain growth that tend to minimize grain surface energy, eventually leading dewetting from the substrate.

Figure 1i displays the statistical data of photovoltaic parameters of PSCs, prepared with a p-i-n architecture that use poly(N,N″-bis-4-butylphenyl-N,N″-bisphenyl)benzidine (PolyTPD) as the hole transport layer (HTL) and phenyl-C_{61}-butyric acid methyl ester (PCBM) as the electron transport layer (ETL), device preparation information is given in the supporting information. We observe an increase of average PCE from 18.7% (untreated, 0 min) to 19.3% (2 min) and 20.0% (5 min) with the treatment, stemming from increase of fill factor (FF) and open-circuit voltage (V_{OC}). However, extending the treatment to 10 min results in PCE drop to 16.6%. We ascribe this to emergence of voids or pinholes acting as potential shunting pathways, and to that fact that increased roughness is likely associated with inhomogeneous coverage of the ETL as the roughness approaches or exceeds the typical PCBM thickness (≈40 nm).[36] Such variation may lead to enhanced charge recombination at open circuit as well as impeded charge extraction, although the neat $MAPbI_3$ film with larger grains and thus fewer grain boundaries indeed show improved PL yield and lifetime after longer treatment

Prof. J. R. Durrant
SPECIFIC IKC
College of Engineering
Swansea University
Swansea SA2 7AX, UK

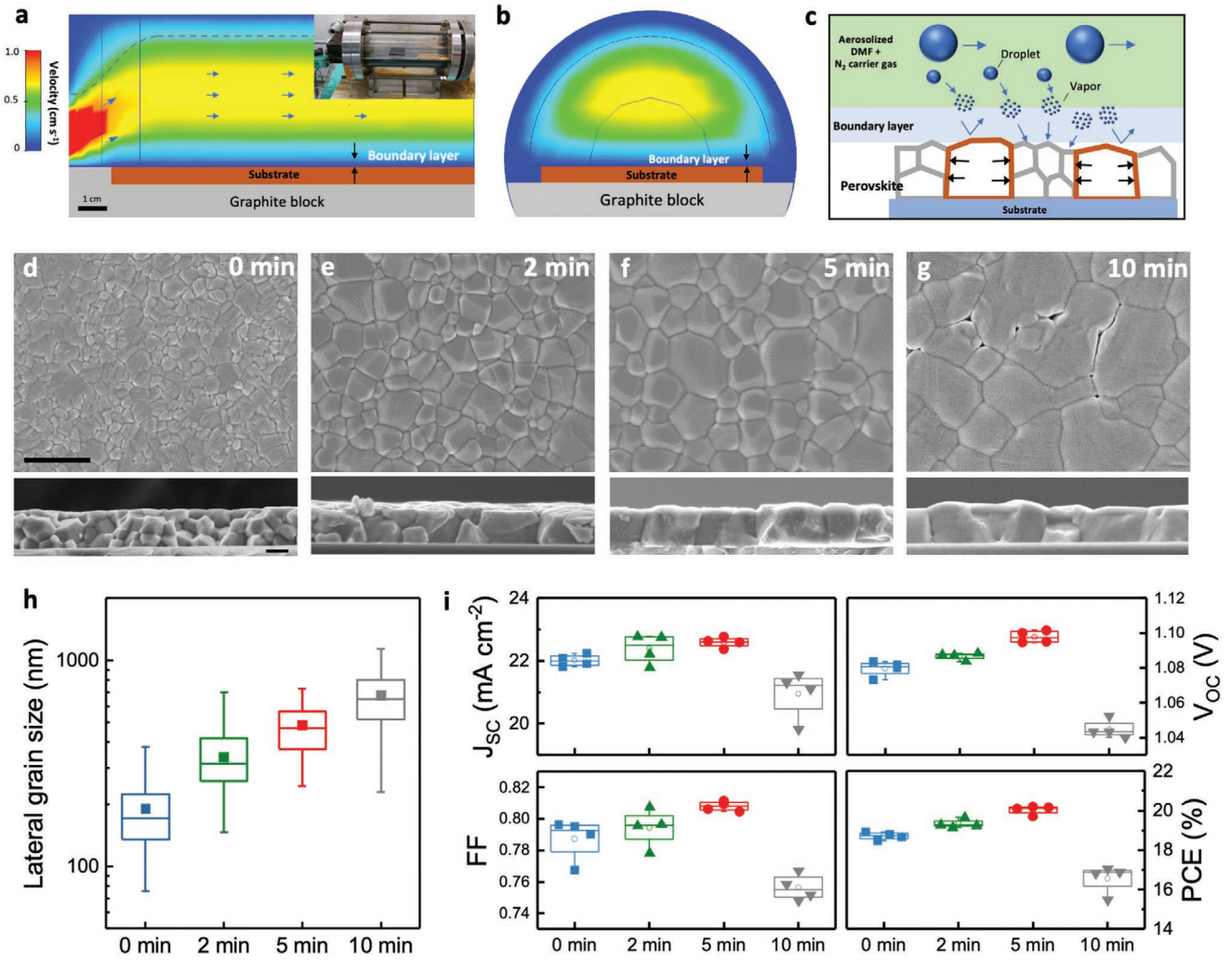

Figure 1. Mechanism of aerosol treatment, tuning film morphology and PSC performance. a) Side view of a 3D CFD simulation of the aerosol flow (N_2 flow rate at 0.5 L min^{-1}) during the aerosol treatment, indicating the velocity distribution of the gas flow. Note the formation of a boundary layer above the substrate. The inset figure shows a photograph of the cylindrical quartz reactor utilized in our study. b) Cross-sectional view of the CFD simulation. c) Schematic drawing showing solvent vapor diffusion through the boundary layer resulting in the preferential consumption of small grains and the subsequent growth of the larger grains, while condensation of solvent droplets is prevented. d–g) Upper panel: surface scanning SEM images of untreated perovskite film (0 min) and perovskites film following aerosol treatment of 2, 5, and 10 min (Scale bars = 1 µm). Lower panel: the corresponding cross-sectional SEM images. (Scale bar = 200 nm). h) Statistical data of lateral grain size distribution measured from the SEM images. i) Photovoltaics parameters (J_{SC}, V_{OC}, FF, and PCE) of typical PSCs at the same time intervals as indicated in (d–g). The data are obtained from reverse-scan *J–V* curves with scanning rate of 50 mV s^{-1}, under simulated AM1.5 illumination at 1 Sun intensity.

(Figure S2d,e, Supporting Information). Therefore, we find that the optimum balance between enhanced grain size and film roughness occurs at 5 min of aerosol exposure.

To highlight the consistency and uniformity of our optimized aerosol treatment, we compare devices with those prepared using solvent vapor annealing (SVA):[37] a method of post-deposition treatment that uses solvent vapor trapped in the volume between a heated surface and an upper boundary—typically an upturned petri dish. Both methods improve device PCE. However, the statistical data show variation of the SVA devices (Figure S3, Supporting Information) are significantly greater, for example a fourfold greater variance in PCE. An analysis of the grain size distribution across a 2.5 × 2.5 cm substrate reveal that the aerosol treated films show a far narrower grain size distribution when compared to those treated by SVA (Figure S4a, Supporting Information). This can be ascribed to solvent movement during SVA being driven by convective flow, resulting in inconsistent and uncontrolled solvent-film interaction, as our CFD simulations indicate (Figure S4b, Supporting Information).

2.2. Microstructural Characterization

Structural analysis using X-ray diffraction, **Figure 2**a, reveals a significant increase in the crystallinity of the aerosol treated films, with the development of a preferential (110) crystallographic orientation. Closer analysis of the (110) diffraction peak at 14.1° 2θ. (Figure 2b), shows a reduction in the peak full width at half maximum (FWHM), which is consistent with aerosol treatment inducing an increase in crystallite size.

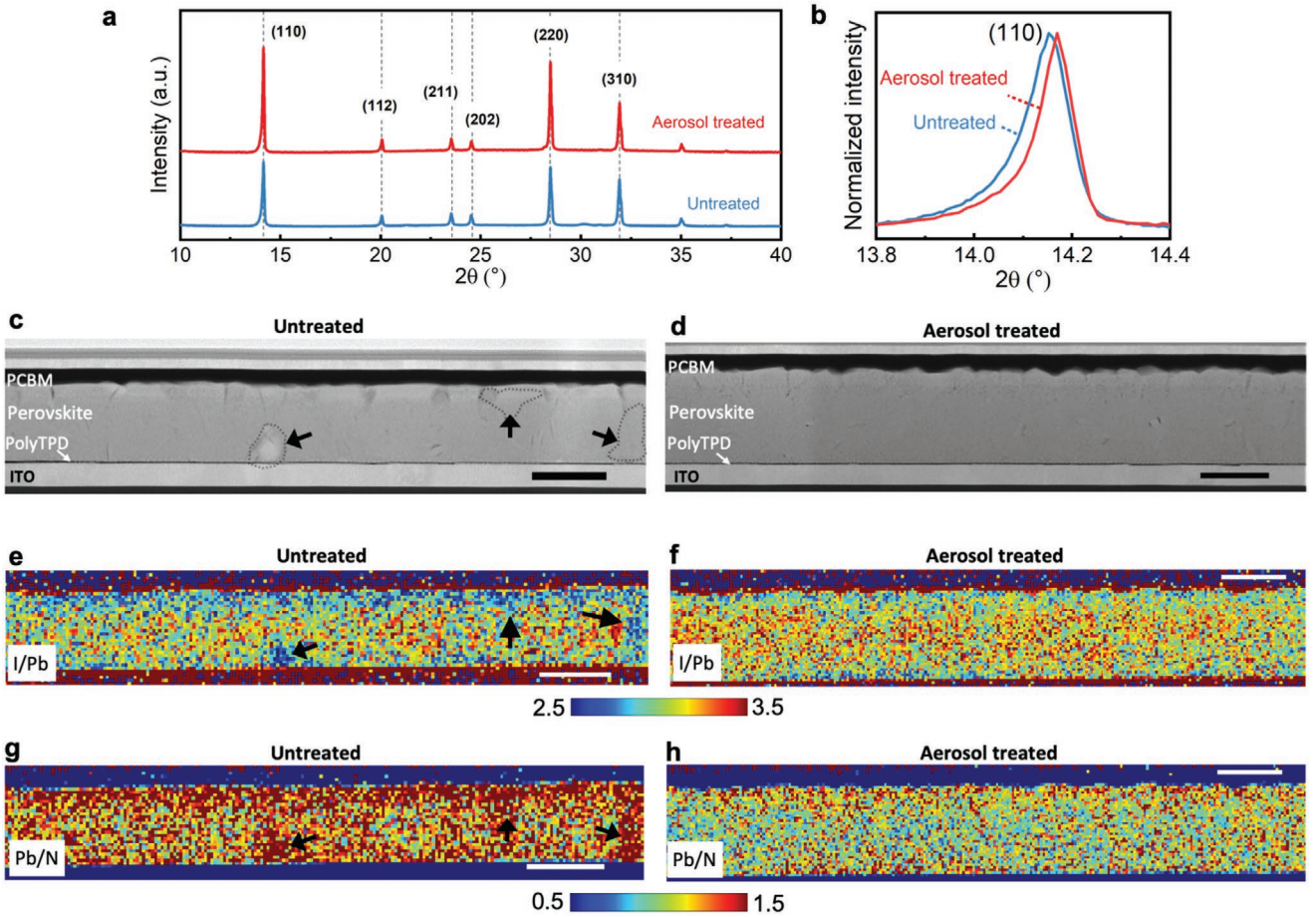

Figure 2. Structural characterization of perovskite films. a) Typical X-ray diffraction (XRD) patterns of the untreated perovskite film and aerosol treated perovskite film. b) Magnified view of the (110) diffraction peaks, note these data are normalized for comparison of peak position and full width at half maximum. c,d) Cross-sectional scanning transmission electron microscopy-high angle annular darkfield (STEM-HAADF) images of complete solar cells (scale bars = 200 nm), e,f) Energy dispersive X-ray spectroscopy (EDX) mapping showing the spatial modulation in the I/Pb concentration ratios (color scale corresponds to deviation from stoichiometry of 3), the thin red strips at the perovskite-PCBM interface in the I/Pb maps are due to electron beam-induced iodine migration towards PCBM.[40] g,h) EDX mapping of Pb/N concentration (color scale corresponds to deviation from stoichiometry of 1). Scale bars in all EDX maps correspond to 200 nm.

Critically, the resolution of SEM analysis in Figure 1d–g does not reveal intragranular effects. Using scanning transmission electron microscopy (STEM) imaging, combined with energy dispersive X-ray (EDX) spectroscopy, we are able to probe nanoscale variations in chemical composition. As these signals are obtained simultaneously, we are also able to directly correlate images and compositional maps. Cross-sectional STEM high-angle annular dark field (HAADF) images of untreated and aerosol treated $MAPbI_3$ films are shown in Figure 2c,d (see also high-magnification images in Figure S5, Supporting Information, where grain boundaries in the untreated film are clearly visible). These images confirm that aerosol treatment increased perovskite layer roughness, in good agreement with the AFM topography maps. EDX maps of these areas are shown in Figure 2e–h. Here we map the spatial distribution of the I:Pb and Pb:N ratios, with the color scale representing a deviation from the stoichiometric 3:1 (I:Pb) and 1:1 (Pb:N) ratios. These maps, and the ratio histograms shown in Figure S6a,b, Supporting Information, show that aerosol treatment improved the $MAPbI_3$ film's compositional homogeneity. Furthermore, a correlative analysis of the images and EDX maps reveal a number of regions in the untreated films in Figure 2c that correspond to regions in the EDX maps where the I:Pb ratio is <3 (Figure 2e) and the Pb:N ratio is >1 (Figure 2g), that is, regions that are rich in Pb. These regions, indicated by arrows, are separated by the order of a few hundred nanometers and are indicative of PbI_2 rich regions, consistent with PbI_2 accumulation at grain boundaries or interfaces.[26] Surface analysis using X-ray photoelectron spectroscopy (XPS), Figure S6 c–f, Supporting Information, also shows an increased concentration of metallic Pb on the surface of the untreated film that has previously been attributed to beam-induced reduction of PbI_2 that already exists in the film.[38] We speculate that the residual PbI_2 is due to the local incomplete conversion of the precursors during the rapid film crystallization followed by loss of the MAI component in the subsequent thermal annealing. Interestingly, Pb enrichment is not observed in the aerosol-treated films, either in the bulk via EDX or on the surface via XPS, despite them being thermally treated, that is, exposed to conditions that are known to promote PbI_2 formation.[26,39] This is largely owing to DMF vapor enabling more efficient mass transfer and grain growth.

The combined STEM and XRD data reveal that, in addition to the grain growth seen in SEM analysis, the aerosol treatment also leads to an improvement in microscale uniformity of the $MAPbI_3$ films. Impurity phases such as PbI_2 are reduced, compositional uniformity increases throughout the film, and crystallites grow and increase their preferred orientation, all of which contribute towards the observed improvements in device performance.

2.3. Spectroscopic and Energetic Characterization

We now probe the electronic and optoelectronic properties of the $MAPbI_3$ films in more detail to further understand the mechanisms through which the above improvements in microstructural properties impact the device performance. Steady-state photoluminescence spectra, **Figure 3**a, shows an approximately

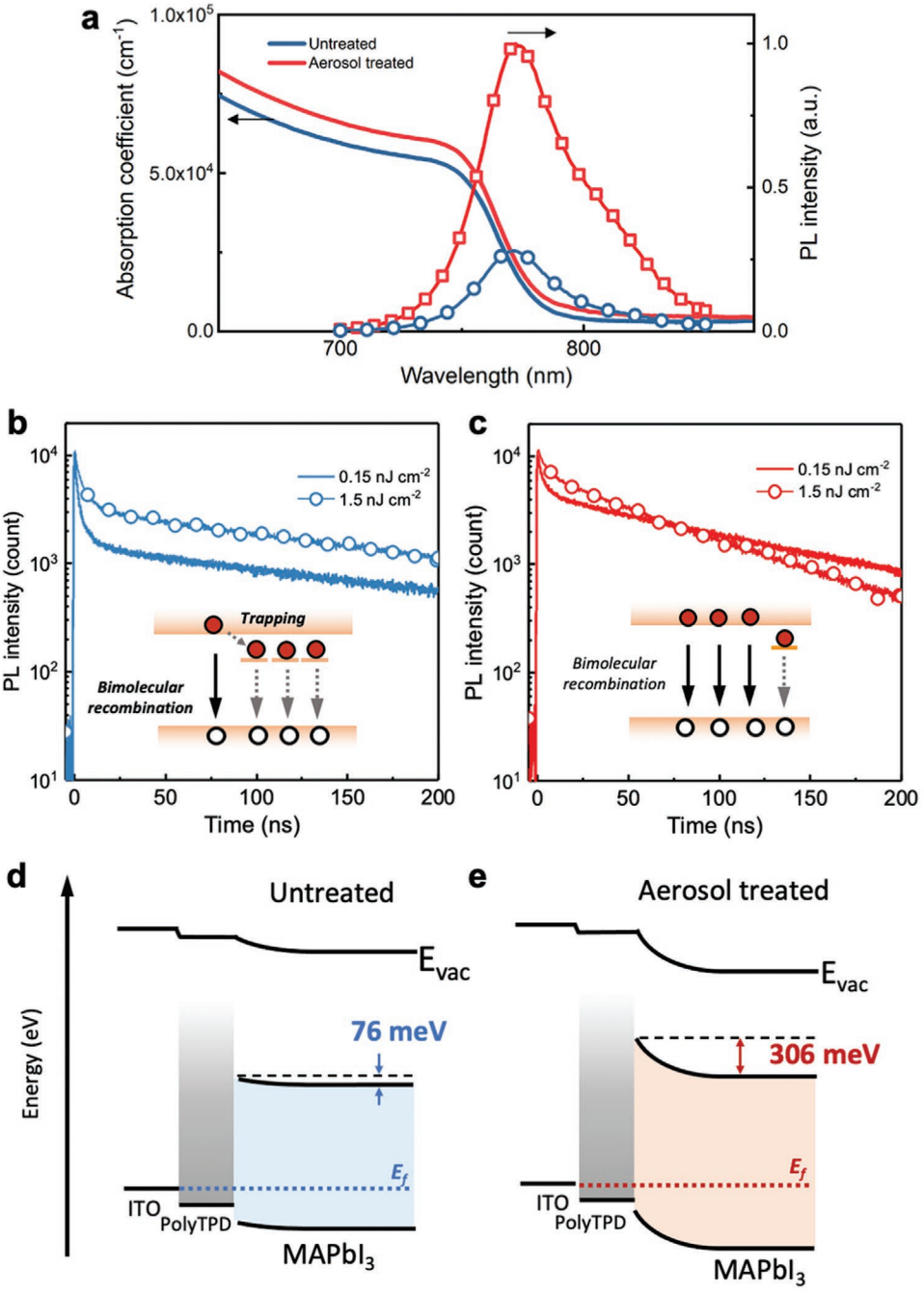

Figure 3. Optoelectronic characterization of perovskite films a) Steady-state PL spectra and absorption spectra of $MAPbI_3$ perovskite films. The PL is collected from a conventional spectrometer with 635-nm excitation at density of 1.5 mW cm^{-2}. b,c) Time-resolved PL spectra of untreated perovskite film (b) and aerosol-treated perovskite film (c), measured with 635-nm excitation at intensity of 0.15 and 1.5 nJ cm^{-2}. Inset illustrations show the reduction in electronic trap states facilitating greater recombination through band-to-band pathway in the aerosol treated films. Schematic images highlighting changes in band bending at the HTL/perovskite interface are shown for d) untreated and e) aerosol treated films.

fourfold increase of PL emission yield of the $MAPbI_3$ film after aerosol treatment. In addition to the increased PL intensity, an asymmetry emerged in the emission, with a shoulder appearing around 800 nm. This correlates with the absorption spectra in the same plot where the aerosol treated $MAPbI_3$ film shows a slight red-shift of absorption onset that is convoluted with some sub-band-gap absorption (see also Figure S7, Supporting Information). We speculate that this is due to in-plane compressive stress applied to some of the grains induced by the lateral grain growth, which may ultimately result in a reduction of bandgap in some local regions.[41] There is also a subtle but distinct increase in absorption coefficient which is associated with the improvement in crystallinity, correlating with our XRD measurements.

Variations in charge recombination mechanisms can be elucidated using time-resolved PL spectroscopy with varying excitation intensity, Figure 3b,c. At low excitation intensity (0.15 nJ cm^{-2}) the decay dynamics are bi-exponential for untreated and aerosol treated films, comprising of a fast initial decay phase (<10 ns), assigned to monomolecular charge trapping, followed by a slow-decay component, attributed to bimolecular recombination.[42] Under such low excitation densities, the bimolecular recombination also takes a pseudo-monomolecular form as the photoexcited charge density is much smaller than background charge density.[43] However, comparing these two samples under 0.15 nJ cm^{-2}, the aerosol treated film shows a two-fold decrease of the fast-phase magnitude, indicating suppression of charge trapping.[44] Increasing the excitation intensity by an order of magnitude to 1.5 nJ cm^{-2}, the decay dynamics of the untreated films remain bi-exponential with a moderate decrease of fast-phase magnitude that has been typically ascribed to partial filling of trap states.[44] In comparison the fast phase disappears almost completely in the aerosol treated film, a strong indication that the majority of photo-excited charge carriers are going through bimolecular recombination pathways.[45] The bi-exponential fits and parameters used for fitting are shown in Figure S8 and Table S1, Supporting Information, respectively.

To explore the impact of this change in defect structure on the energetics of the films, contact potential difference (CPD) measurements were obtained by scanning Kelvin probe force microscopy over 3 × 3 μm areas, Figure S9, Supporting Information.[46] The spatially averaged contact potential difference (CPD) data show a shift of –76 meV for the untreated films and –306 meV for the aerosol treated films relative to the ITO reference. This shows that the aerosol treatment enhances HTL/perovskite interfacial band bending by 230 meV in the direction favorable for hole extraction, Figure 3d,e. The data also reveal a decrease in work function in the aerosol treated perovskite following aerosol treatment suggesting that there are fewer ionic defects acting as p-type dopants in the aerosol treated films, for example, Pb vacancies,[47] consistent with all other analysis, although we note that the p-doping can also be influenced by the underlying HTL.[48]

2.4. Device Stability and Large-Area Devices

Several strategies focusing on active layer crystallinity and its impact on device stability have been reported.[14,15] It is therefore interesting to consider how the improvements in crystallinity and reductions in defect density influence operational stability. **Figure 4**a shows how device PCE, measured by maximum power point (MPP) tracking at 25 °C in N_2, varies between an untreated and aerosol treated device. The stability of the aerosol treated device is enhanced greatly, particularly in the first 200–300 h, with a 10% ($t_{0.9}$) reduction in PCE occurring after 700 h. In sharp contrast, the untreated device exhibits a rapid drop of PCE, some 5% in the first 20 h, and reaches $t_{0.9}$ after ≈220 h. Intriguingly, in both sets of devices the rate of PCE decline after around 250 h are similar, likely due to the intrinsic instability of MA based perovskites or diffusion of Cu electrode through bathocuproine (BCP) and PCBM layers.[49] Considering that the protocol of stability measurements can influence the results,[50] Figure 4b compares the evolution of PCEs under the same environment but holding devices at open circuit and periodically obtaining *J–V* data. Consistent with MPP tracking data, there is a remarkable enhancement of device stability particularly in the first 200 h. We believe this is due to a combination of improved phase purity, thus elimination of local residual PbI_2 that prevents the nucleation and growth of PbI_2 as a degradation product. Stability measurements in ambient conditions (Figure S10, Supporting Information) also show improvements for the aerosol treated devices owing that increased crystallinity and grain size may retard O_2/H_2O ingress,[51] although, as anticipated, the overall operational lifetime is much shorter in these conditions.

In addition to stability, scale-up of device area is also critical for future implementation of PSCs. Here we consider the impact of aerosol treatment as device area is increased, Figure 4c,d. Using a single 2 × 2 cm substrate containing two devices with areas of 0.25 and 1.025 cm^2 (inset of Figure 4c), we study the scaling effect of untreated and aerosol treated films. In the aerosol treated films, the measured PCE reduces from 18.5% to 17.6% as the area increases from 0.25 to 1.025 cm^2: a change of only 4.6%. In contrast, for the untreated device PCE falls from 18.1% to 16.3%, that is, a change of around 10% when scaled-up. The reduction of PCE loss when device area increases, highlighted in the inset of Figure 4d, is ascribed to the combination of micro-scale structural improvements and macroscopic improvements in uniformity induced by the aerosol treatment, eliminating local photoinactive regions or blocking shunt pathways as grain size grows.[52]

2.5. Demonstrating Aerosol Treatment Universality

So far, we have demonstrated that aerosol assisted solvent treatment is an effective technique for improving the efficiency and reproducibility of $MAPbI_3$ PSCs with a single p-i-n architecture. However, numerous charge extraction layers and alternative architectures with high efficiencies have been demonstrated in the literature.[53,54] In order to highlight the universality of our aerosol treatment, we investigate its application to a wide range of device configurations, specifically: i) $MAPbI_3$ devices prepared with active layer thicknesses up to 1300nm; ii) devices prepared with alternative HTLs and HTL-free devices; iii) methylammonium-free (formamidinium-caesium) double cation perovskites; and iv) devices prepared in the n-i-p architecture.

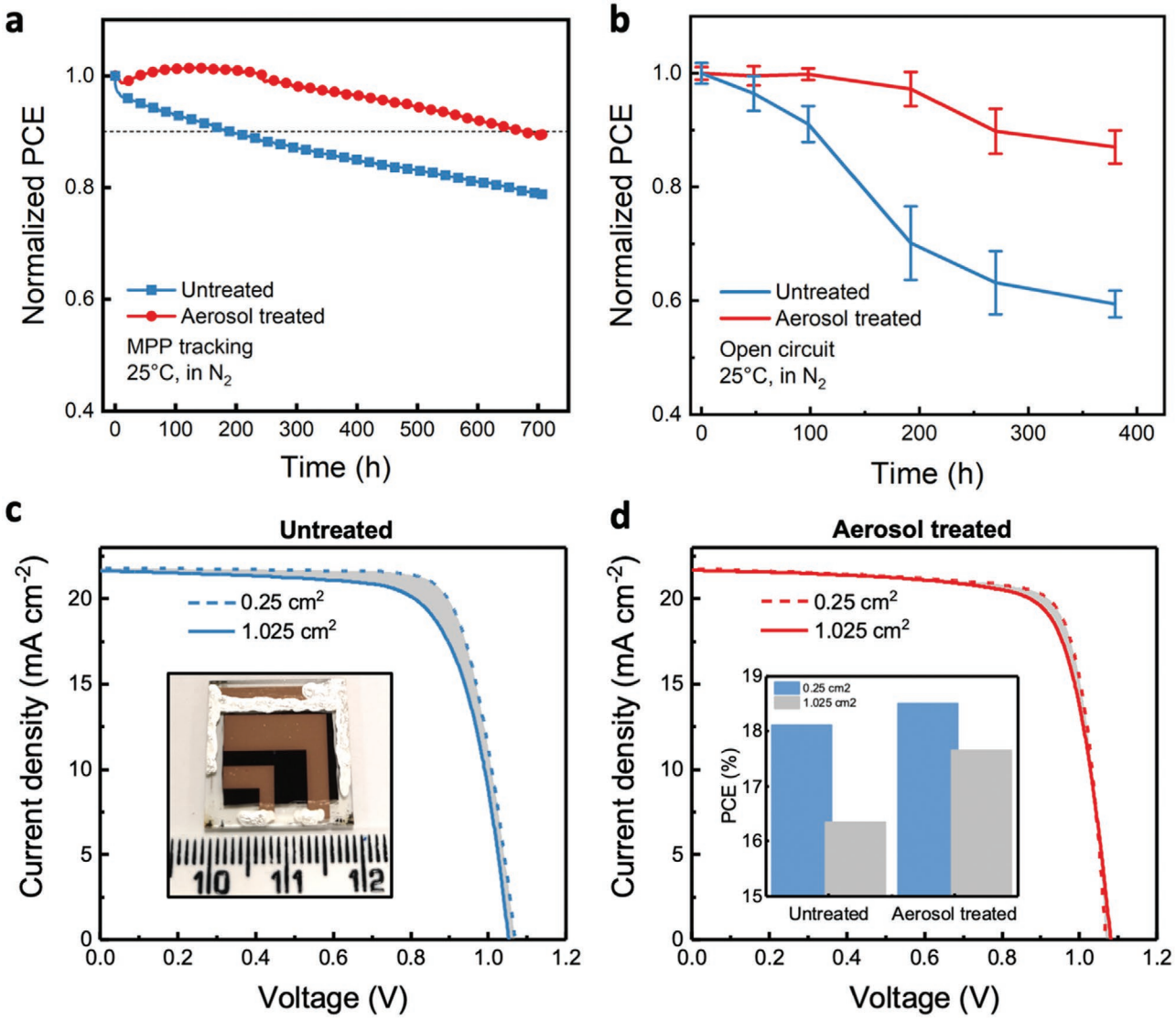

Figure 4. Stability measurement and device scale-up. a) Evolution of PCE measured by holding the PSCs at maximum power point. Here the PCEs are normalized to the initial values obtained for the untreated and aerosol treated devices, 18.3% and 19.3% respectively. b) Evolution of PCE measured by holding the PSCs at open circuit and periodically scanning *J*–*V* curves. The PCEs are measured from four devices and are normalized to initial value of 18.2 ± 0.3% (untreated) and 18.9 ± 0.2% (aerosol treated). c,d) *J*–*V* curves of the two pixels with areas of 0.25 and 1.025 cm^2 on the same substrate, measured with reverse-scan direction at rate of 50 mV s^{-1}, under simulated AM1.5 illumination of 1 Sun intensity. The inset figure in (c) shows a photograph of a device with the two active areas visible. The inset figure in (d) shows a bar chart that highlights the change of PCE for the different device areas in untreated and aerosol treated conditions.

2.5.1. Increased Active Layer Thickness

The typical active layer thickness of high-performing PSCs is in the region of 300–500 nm. Whilst perovskite single crystals have shown diffusion lengths well in excess of this length,[55] GBs and the resulting trap states have limited the optimum thickness used in devices. This limits the maximum amount of light the active layer can absorb and constrains thickness tolerances, making large-scale deposition more challenging. Therefore, considering the reduction in GBs and improvement in film properties, we investigated the effect of our aerosol treatment on thicker perovskite films of 900 and 1300 nm. **Figure 5**a shows cross-sectional SEM images of untreated and aerosol treated $MAPbI_3$ films of nominal thickness 500, 900, and 1300 nm. In the untreated films, the micrographs reveal vertically stacked grains with grain size being largely insensitive to film thickness. Following aerosol exposure there is a significant change in the $MAPbI_3$ grain size and shape with the small grains of the untreated films being replaced by monolithic grains that extend the entire film thickness; despite the considerable increase in film thickness we see no evidence of horizontal grain boundaries following aerosol treatment. The grain size in the aerosol treated films now shows a dependence on film thickness, with larger grains being formed in thicker films. This reflects the significant structural reorganization and recrystallization seen in Figure 2 and demonstrates that it occurs throughout the film thickness even in films up to 1300 nm thick.

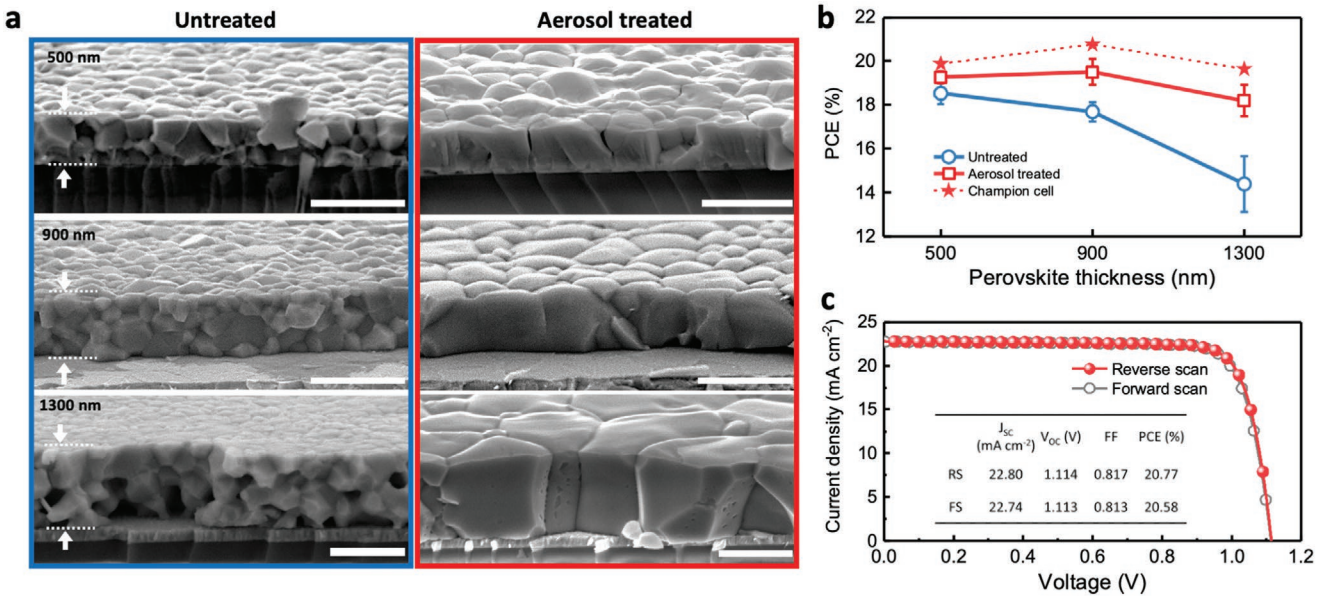

Figure 5. Thickness dependent microstructure and photovoltaic properties a) Cross-sectional scanning electron microscopy (SEM) images of untreated (left column) and aerosol treated (right column) perovskite films of different thickness (Scale bars = 1 µm). b) Measured PCE values for devices prepared from $MAPbI_3$ films of 500, 900, and 1300 nm. Also shown are the single device data for the champion cell at each thickness. c) *J–V* data, forward (FS) and reverse scan (RS) for the champion device with all device parameters shown in inset table.

Figure 5b shows the PCE of p-i-n structured devices for untreated and aerosol treated films with three active layer thicknesses. In the untreated films, increasing thickness results in a reduction of PCE. These thickness-dependent losses stem from reductions in short circuit current density (J_{SC}) and fill factor (FF) (Figure S11, Supporting Information) due to the horizontal grain boundaries impeding charge transport. However, these losses are minimal in aerosol treated devices. Aerosol treatment significantly improves all device characteristics with the best performing devices now being those with an active layer thickness of 900 nm, whilst 1300 nm devices exhibit performance metrics only slightly below their 500 nm counterparts. The champion 900 nm device, Figure 5c, has a J_{SC} = 22.8 mA cm^{-2}, V_{OC} = 1.11 V, FF = 0.81, and PCE = 20.77% with minimal hysteresis and an integrated external quantum efficiency (EQE) of 22.4 mA cm^{-2} (correlating with the measured J_{SC}), Figure S12, Supporting Information. By mediating ionic and/or electronic defects, the aerosol treatment allows for use of thick absorber layers that can improve light harvesting.[56] This not only gives rise to higher PCE of the champion device but is also favorable for large-scale manufacturing of PSCs, for example, printing, where thicker absorber layers are typically employed to overcome associated defects such as pinholes.

Structural characterization of the thicker $MAPbI_3$ films using X-ray diffraction show the anticipated changes upon aerosol treatment, that is, an increase in the degree of crystallinity, an increase in grain size and the development of a preferred (110) orientation, Figure S13, Supporting Information. Closer analysis of the (110) diffraction peaks reveals a peak shift to higher 2θ value after aerosol treatment, the magnitude of which increases with film thickness. Similar shifts are seen in other diffraction peaks indicating a reduction in the size of the lattice. Overall, these results show that the aerosol treatment can be readily applied to perovskite films with a large variation of film thickness, resulting in consistent improvement of film quality and thus high-performing devices.

2.5.2. Hole Transport Layer (HTL) Variation and HTL-Free Devices

Thus far we have demonstrated the effectiveness of aerosol treatment using PolyTPD as the HTL owing to the high-performing devices produced. However, PolyTPD creates processing challenges due to its hydrophobic nature.[57] As an alternative HTL we consider p-i-n devices with hydrophilic poly(3,4-ethylenedioxythiophene)-poly(styrenesulfonate) (PEDOT:PSS), as well as HTL-free devices. Both architectures are attractive owing to ease of preparation and reduced materials cost, particularly benefiting high-volume manufacturing, but normally yield lower performing devices.[58]

Figure 6a shows a schematic energy diagram of the p-i-n PSCs with different HTLs, while Figure 6b shows how the PCE varies when the HTLs are varied. The PolyTPD devices outperform those prepared using PEDOT:PSS, which is anticipated. However, the enhancement of PCE following aerosol treatment is much greater for PEDOT:PSS devices where the average PCE increased from 13.5 ± 0.4%, to 17.6 ± 0.4%, compared to 18.7 ± 0.4% to 19.7 ± 0.3% for PolyTPD devices. The PCE of HTL-free devices increases by an even greater factor after aerosol treatment, from 9.6 ± 0.5% to 15.4 ± 0.4%, comparable to the best-performing dopant-free, HTL-free devices previously reported.[59] *J–V* curves, Figure 6c, as well as the photovoltaic parameters, Figure S14, Supporting Information, show that the improved PCE is driven by considerable improvement of V_{OC} and FF for the HTL-free device, and mainly by improvement of V_{OC} for the PEDOT:PSS device. Here the combination of increased film

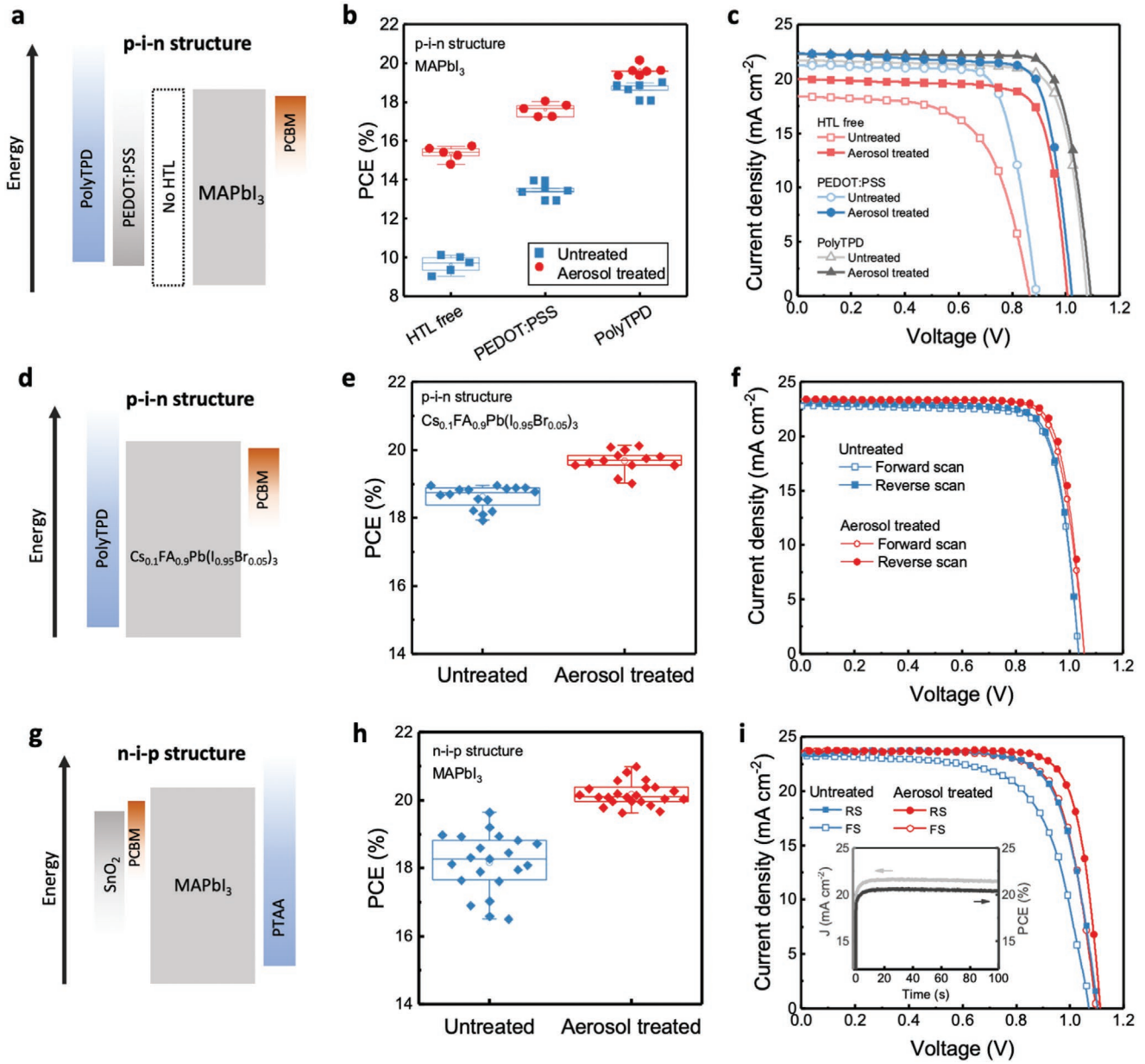

Figure 6. Alternative device configurations and architectures. Panels show from left to right: schematic illustrations of flat-band energy level diagrams, statistical device PCE data and typical *J–V* curves for a–c) p-i-n PSCs with different HTLs, d–f) p-i-n PSCs using $Cs_{0.1}FA_{0.9}Pb(I_{0.95}Br_{0.05})_3$ (CsFA) as an active layer, g–i) n-i-p PSCs (inset of figure (i) shows the steady-state power output). In (c), only reverse scans of *J–V* curves are shown. In (f) and (i), both forward scans (FS) and reverse scans (RS) of *J–V* curves are shown. Scan speed is 50 mV s^{-1} in all cases.

crystallinity, reduced ionic defects and the reduction in p-doping of the perovskite collectively create more favorable band bending at HTL/perovskite or ITO/perovskite interface that facilitates hole extraction and reduces surface recombination.[60]

2.5.3. Methylammonium-Free Double Cation Perovskites

To demonstrate the true universality of our aerosol treatment we turn to investigate formamidinium (FA)-based perovskites. These perovskites are attractive due to their excellent thermal stability,[61] although their PCEs are normally lower that MA- or MA-FA-based counterparts.[62] We fabricated the FA-perovskite films with a nominal composition of $Cs_{0.1}FA_{0.9}Pb(I_{0.95}Br_{0.05})$ with our standard p-i-n architecture, Figure 6d, where incorporation of caesium (Cs) alongside FA is reported to stabilize the perovskite structure.[63] Statistics of PCE, Figure 6e, show an improvement in the average PCE, from 18.6 ± 0.3% to 19.7 ± 0.3% after aerosol treatment. The measured photovoltaic parameters shown in Figure S15a–c, Supporting Information, reveals that such improvement is driven mainly by an increase of V_{OC} and FF. *J–V* curves of the champion device, Figure 6f, shows a PCE of 19.0% for the untreated device and 20.1% for the aerosol treated device, with minimal *J–V* hysteresis seen

in both devices. The aerosol treated device has an integrated external quantum efficiency (EQE) of 23.0 mA cm^{-2} that correlates well with the measured J_{SC}, Figure S16, Supporting Information. Characterization of the $Cs_{0.1}FA_{0.9}Pb(I_{0.95}Br_{0.05})$ films, Figure S17, Supporting Information, show an increase of grain size and the formation of monolithic grains, combined with improvements in crystallinity after aerosol treatment is implemented, which correlates to a reduction of trap states in these films. These are all consistent with the modifications that have been observed on $MAPbI_3$ films.

2.5.4. n-i-p Architectures

To conclude, we consider devices prepared in the n-i-p configuration that most state-of-the-art PSCs have adopted.[5,12,19,64] Figure 6g shows a schematic illustration of the energy level diagram of the devices, where a nanoparticle SnO_2/PCBM bilayer is used as the ETL and poly[bis(4-phenyl)(2,4,6-trimethylphenyl) amine (PTAA) as an HTL. Analysis of the PCE data, Figure 6h, and other device characteristics, Figure S15d–f, Supporting Information, show the aerosol treatment significantly improves device. In addition to the average PCE values increasing from 18.2 ± 0.9% (champion 19.2%) to 20.2 ± 0.3% (champion 21.0%) following aerosol treatment, the spread in all characteristics are also reduced, that is, aerosol treatment creates better performing devices with statistically less variance in performance. One drawback of the n-i-p structure is that hysteresis is generally more problematic than in p-i-n analogues. Figure 6i shows *J–V* curves for the champion untreated and aerosol treated devices, where it is apparent that hysteresis is reduced in the aerosol treated device, indicative of a reduction in ionic defects. Despite the moderate *J–V* hysteresis even after aerosol treatment, the steady-state power output measurement (inset in Figure 6i) shows a stabilized PCE of 20.5% when the device is held near the MPP (0.952 V).

3. Conclusion

We have introduced an innovative post-deposition treatment universally applicable to a wide range of PSC configurations and architectures. The methodology yields significant improvements in device efficiency and operational stability, coupled with a reduction in inherent batch-to-batch variability in all performance metrics. Such improvements are achieved following an aerosol-induced recrystallization of solution deposited $MAPbI_3$ thin films that results in a significant enlargement and improved homogeneity of grain size.

The aerosol treatment is demonstrated as being universally suitable for a range of active layer thicknesses, hole transport layers, architectures, active areas, and perovskite compositions. Significantly, all benefits can be obtained without modification of existing deposition methods or the introduction of compositional modulation through additives. In addition to increasing grain size and crystallinity, our process enables the elimination of PbI_2 that may be present due to either thermally-induced degradation or remaining unreacted precursor, improves the chemical homogeneity of the perovskite and significantly reduces ionic and electronic defects.

The synergistic improvements in structure, composition, and defect chemistry allow for the preparation of champion p-i-n $MAPbI_3$ devices with a PCE of 20.8%, $MAPbI_3$ devices with active areas exceeding 1 cm^2 with a PCE of 17.6% and remarkably HTL free devices with PCEs >15%. Importantly, this method is scalable, and we have shown that it can improve large-area uniformity and improve the efficiency of thicker active layers. All of these features make this technique highly suitable for large-volume manufacturing of PSCs. In fact, whilst we have demonstrated this on a lab-scale reactor (Figure S1, Supporting Information), this reactor is designed to pilot chemical vapor deposition processes for future scale-up to the commercial (meters+) scale. Furthermore, the highly controlled nature of this technique could be further applied to the fundamental study of perovskite materials, where the controlled grain growth, defect and dopant tuning could allow property-performance relationships to be studied in greater detail in the future. Therefore, the simplicity, versatility, and reproducibility of our methodology will enable its immediate uptake by researchers in the field to further study these interesting properties and enable improvements in future devices.

Supporting Information

Supporting Information is available from the Wiley Online Library or from the author.

Acknowledgements

T.D. and S.R.R. contributed equally to the work. The authors thank the EPSRC Plastic Electronics CDT (EP/L016702/1) for financial support and provision of equipment resource. M.A.M. and J.R.D. acknowledge the Global Research Laboratory (GRL) Program through the National Research Foundation of Korea (NRF) funded by the Ministry of Science and ICT (NRF-2017K1A1A2013153). T.D. gratefully acknowledges the Stephen and Anna Hui Scholarship (Imperial College London) for financially supporting his doctoral studies. F.U.K. thanks the Jardine Foundation and Cambridge Trust for a doctoral scholarship. Finally, T.J.M would like to thank the Royal Commission for the 1851 Exhibition for their financial support through an 1851 Research Fellowship.

Conflict of Interest

The authors declare no conflict of interest.

Data Availability Statement

Research data are not shared.

Keywords

grain growth, large-area, MAPI, perovskite solar cells, post-deposition treatment

Received: May 6, 2021
Revised: June 13, 2021
Published online:

[1] A. Kojima, K. Teshima, Y. Shirai, T. Miyasaka, *J. Am. Chem. Soc.* **2009**, *131*, 6050.
[2] R. F. Service, *Science* **2019**, *364*, 918.
[3] S. F. Leung, K. T. Ho, P. K. Kung, V. K. S. Hsiao, H. N. Alshareef, Z. L. Wang, J. H. He, *Adv. Mater.* **2018**, *30*, 1704611.
[4] J. H. L. Ngai, J. K. W. Ho, R. K. H. Chan, S. H. Cheung, L. M. Leung, S. K. So, *RSC Adv.* **2017**, *7*, 49353.
[5] N. J. Jeon, J. H. Noh, Y. C. Kim, W. S. Yang, S. Ryu, S. Il Seok, *Nat. Mater.* **2014**, *13*, 897.
[6] T. Du, C. H. Burgess, C.-T. Lin, F. Eisner, J. Kim, S. Xu, H. Kang, J. R. Durrant, M. A. McLachlan, *Adv. Funct. Mater.* **2018**, *28*, 1803943.
[7] N. J. Jeon, J. H. Noh, W. S. Yang, Y. C. Kim, S. Ryu, J. Seo, S. Il Seok, *Nature* **2015**, *517*, 476.
[8] D. P. McMeekin, G. Sadoughi, W. Rehman, G. E. Eperon, M. Saliba, M. T. Hörantner, A. Haghighirad, N. Sakai, L. Korte, B. Rech, M. B. Johnston, L. M. Herz, H. J. Snaith, *Science* **2016**, *351*, 151.
[9] T. Jesper Jacobsson, J. P. Correa-Baena, M. Pazoki, M. Saliba, K. Schenk, M. Grätzel, A. Hagfeldt, *Energy Environ. Sci.* **2016**, *9*, 1706.
[10] W. Yan, S. Ye, Y. Li, W. Sun, H. Rao, Z. Liu, Z. Bian, C. Huang, *Adv. Energy Mater.* **2016**, *6*, 1600474.
[11] T. Du, W. Xu, M. Daboczi, J. Kim, S. Xu, C.-T. Lin, H. Kang, K. Lee, M. J. Heeney, J.-S. Kim, J. R. Durrant, M. A. McLachlan, *J. Mater. Chem. A* **2019**, *7*, 18971.
[12] S. Yang, S. Chen, E. Mosconi, Y. Fang, X. Xiao, C. Wang, Y. Zhou, Z. Yu, J. Zhao, Y. Gao, F. De Angelis, J. Huang, *Science* **2019**, *365*, 473.
[13] M. Stolterfoht, C. M. Wolff, J. A. Márquez, S. Zhang, C. J. Hages, D. Rothhardt, S. Albrecht, P. L. Burn, P. Meredith, T. Unold, D. Neher, *Nat. Energy* **2018**, *3*, 847.
[14] X. Zheng, B. Chen, J. Dai, Y. Fang, Y. Bai, Y. Lin, H. Wei, X. C. Zeng, J. Huang, *Nat. Energy* **2017**, *2*, 17102.
[15] S. Bai, P. Da, C. Li, Z. Wang, Z. Yuan, F. Fu, M. Kawecki, X. Liu, N. Sakai, J. T.-W. Wang, S. Huettner, S. Buecheler, M. Fahlman, F. Gao, H. J. Snaith, *Nature* **2019**, *571*, 245.
[16] T. H. Han, J. W. Lee, C. Choi, S. Tan, C. Lee, Y. Zhao, Z. Dai, N. De Marco, S. J. Lee, S. H. Bae, Y. Yuan, H. M. Lee, Y. Huang, Y. Yang, *Nat. Commun.* **2019**, *10*, 520.
[17] M. Abdi-Jalebi, Z. Andaji-Garmaroudi, S. Cacovich, C. Stavrakas, B. Philippe, J. M. Richter, M. Alsari, E. P. Booker, E. M. Hutter, A. J. Pearson, S. Lilliu, T. J. Savenije, H. Rensmo, G. Divitini, C. Ducati, R. H. Friend, S. D. Stranks, *Nature* **2018**, *555*, 497.
[18] C. Lin, J. Lee, J. Kim, T. J. Macdonald, J. Ngiam, B. Xu, M. Daboczi, W. Xu, S. Pont, B. Park, H. Kang, J. Kim, D. J. Payne, K. Lee, J. R. Durrant, M. A. McLachlan, *Adv. Funct. Mater.* **2020**, *30*, 1906763.
[19] D. Bi, C. Yi, J. Luo, J. D. Décoppet, F. Zhang, S. M. Zakeeruddin, X. Li, A. Hagfeldt, M. Grätzel, *Nat. Energy* **2016**, *1*, 16142.
[20] J. M. Ball, A. Petrozza, *Nat. Energy* **2016**, *1*, 16149.
[21] W.-J. Yin, T. Shi, Y. Yan, *Appl. Phys. Lett.* **2014**, *104*, 063903.
[22] Y. Shao, Y. Fang, T. Li, Q. Wang, Q. Dong, Y. Deng, Y. Yuan, H. Wei, M. Wang, A. Gruverman, J. Shield, J. Huang, *Energy Environ. Sci.* **2016**, *9*, 1752.
[23] T. S. Sherkar, C. Momblona, L. Gil-Escrig, J. Ávila, M. Sessolo, H. J. Bolink, L. J. A. Koster, *ACS Energy Lett.* **2017**, *2*, 1214.
[24] J. P. Correa-Baena, M. Anaya, G. Lozano, W. Tress, K. Domanski, M. Saliba, T. Matsui, T. J. Jacobsson, M. E. Calvo, A. Abate, M. Grätzel, H. Míguez, A. Hagfeldt, *Adv. Mater.* **2016**, *28*, 5031.
[25] N. Aristidou, C. Eames, I. Sanchez-Molina, X. Bu, J. Kosco, M. Saiful Islam, S. A. Haque, *Nat. Commun.* **2017**, *8*, 15218.
[26] T. Du, C. H. Burgess, J. Kim, J. Zhang, J. R. Durrant, M. A. McLachlan, *Sustainable Energy Fuels* **2017**, *1*, 119.
[27] D.-Y. Son, J.-W. Lee, Y. J. Choi, I.-H. Jang, S. Lee, P. J. Yoo, H. Shin, N. Ahn, M. Choi, D. Kim, N.-G. Park, H.-S. Kim, A. Kojima, K. Teshima, Y. Shirai, T. Miyasaka, J.-H. Im, C.-R. Lee, J.-W. Lee, S.-W. Park, N.-G. Park, M. Liu, M. B. Johnston, H. J. Snaith, J. Burschka, S. D. Stranks, G. Xing, D. Shi, Q. Dong, et al., *Nat. Energy* **2016**, *1*, 16081.
[28] Y. Bai, Y. Lin, L. Ren, X. Shi, E. Strounina, Y. Deng, Q. Wang, Y. Fang, X. Zheng, Y. Lin, Z. G. Chen, Y. Du, L. Wang, J. Huang, *ACS Energy Lett.* **2019**, *4*, 1231.
[29] P. Docampo, F. C. Hanusch, N. Giesbrecht, P. Angloher, A. Ivanova, T. Bein, *APL Mater.* **2014**, *2*, 081508.
[30] X. Zheng, Y. Hou, C. Bao, J. Yin, F. Yuan, Z. Huang, K. Song, J. Liu, J. Troughton, N. Gasparini, C. Zhou, Y. Lin, D. J. Xue, B. Chen, A. K. Johnston, N. Wei, M. N. Hedhili, M. Wei, A. Y. Alsalloum, P. Maity, B. Turedi, C. Yang, D. Baran, T. D. Anthopoulos, Y. Han, Z. H. Lu, O. F. Mohammed, F. Gao, E. H. Sargent, O. M. Bakr, *Nat. Energy* **2020**, *5*, 131.
[31] W. Zhang, S. Pathak, N. Sakai, T. Stergiopoulos, P. K. Nayak, N. K. Noel, A. A. Haghighirad, V. M. Burlakov, D. W. Dequilettes, A. Sadhanala, W. Li, L. Wang, D. S. Ginger, R. H. Friend, H. J. Snaith, *Nat. Commun.* **2015**, *6*, 10030.
[32] C. Bi, Q. Wang, Y. Shao, Y. Yuan, Z. Xiao, J. Huang, *Nat. Commun.* **2015**, *6*, 7747.
[33] Z. Chen, B. Turedi, A. Y. Alsalloum, C. Yang, X. Zheng, I. Gereige, A. Alsaggaf, O. F. Mohammed, O. M. Bakr, *ACS Energy Lett.* **2019**, *4*, 1258.
[34] Z. Chen, Q. Dong, Y. Liu, C. Bao, Y. Fang, Y. Lin, S. Tang, Q. Wang, X. Xiao, Y. Bai, Y. Deng, J. Huang, *Nat. Commun.* **2017**, *8*, 1890.
[35] P. W. Voorhees, *J. Stat. Phys.* **1985**, *38*, 231.
[36] J.-W. Lee, D.-K. Lee, D.-N. Jeong, N.-G. Park, *Adv. Funct. Mater.* **2019**, *29*, 1807047.
[37] J. Min, N. S. Güldal, J. Guo, C. Fang, X. Jiao, H. Hu, T. Heumüller, H. Ade, C. J. Brabec, *J. Mater. Chem. A* **2017**, *5*, 18101.
[38] D. W. deQuilettes, W. Zhang, V. M. Burlakov, D. J. Graham, T. Leijtens, A. Osherov, V. Bulović, H. J. Snaith, D. S. Ginger, S. D. Stranks, *Nat. Commun.* **2016**, *7*, 11683.
[39] J. D. McGettrick, K. Hooper, A. Pockett, J. Baker, J. Troughton, M. Carnie, T. Watson, *Mater. Lett.* **2019**, *251*, 98.
[40] F. U. Kosasih, S. Cacovich, G. Divitini, C. Ducati, *Small Methods* **2021**, *5*, 2000835.
[41] L. Kong, G. Liua, J. Gong, Q. Hu, R. D. Schaller, P. Dera, D. Zhang, Z. Liu, W. Yang, K. Zhu, Y. Tang, C. Wang, S. H. Wei, T. Xu, H. K. Mao, *Proc. Natl. Acad. Sci. USA* **2016**, *113*, 8910.
[42] X. Wen, Y. Feng, S. Huang, F. Huang, Y. Cheng, M. Green, A. Hobaillie, *J. Mater. Chem. C* **2015**, *4*, 793.
[43] C. S. Ponseca, E. M. Hutter, P. Piatkowski, B. Cohen, T. Pascher, A. Douhal, A. Yartsev, V. Sundström, T. J. Savenije, *J. Am. Chem. Soc.* **2015**, *137*, 16043.
[44] J. Kim, R. Godin, S. D. Dimitrov, T. Du, D. Bryant, M. A. McLachlan, J. R. Durrant, *Adv. Energy Mater.* **2018**, 1802474.
[45] S. D. Stranks, V. M. Burlakov, T. Leijtens, J. M. Ball, A. Goriely, H. J. Snaith, *Phys. Rev. Appl.* **2014**, *2*, 034007.
[46] M. Daboczi, I. Hamilton, S. Xu, J. Luke, S. Limbu, J. Lee, M. A. McLachlan, K. Lee, J. R. Durrant, I. D. Baikie, J. S. Kim, *ACS Appl. Mater. Interfaces* **2019**, *11*, 46808.
[47] C. Li, A. Guerrero, S. Huettner, J. Bisquert, *Nat. Commun.* **2018**, *9*, 5113.
[48] J. R. Harwell, T. K. Baikie, I. D. Baikie, J. L. Payne, C. Ni, J. T. S. Irvine, G. A. Turnbull, I. D. W. Samuel, *Phys. Chem. Chem. Phys.* **2016**, *18*, 19738.
[49] C.-T. Lin, J. Ngiam, S. Xu, Y.-H. Chang, T. Du, T. J. Macdonald, J. Durrant, M. McLachlan, *J. Mater. Chem. A* **2020**, *8*, 8684.
[50] K. Domanski, E. A. Alharbi, A. Hagfeldt, M. Grätzel, W. Tress, *Nat. Energy* **2018**, *3*, 61.
[51] H. J. Yen, P. W. Liang, C. C. Chueh, Z. Yang, A. K. Y. Jen, H. L. Wang, *ACS Appl. Mater. Interfaces* **2016**, *8*, 14513.
[52] Z. Li, T. R. Klein, D. H. Kim, M. Yang, J. J. Berry, M. F. A. M. Van Hest, K. Zhu, *Nat. Rev. Mater.* **2018**, *3*, 18017.

[53] D. Prochowicz, R. Runjhun, M. M. Tavakoli, P. Yadav, M. Saski, A. Q. Alanazi, D. J. Kubicki, Z. Kaszkur, S. M. Zakeeruddin, J. Lewiński, M. Grätzel, *Chem. Mater.* **2019**, *31*, 1620.
[54] H. S. Kim, A. Hagfeldt, N. G. Park, *Chem. Commun.* **2019**, *55*, 1192.
[55] S. D. Stranks, S. D. Stranks, G. E. Eperon, G. Grancini, C. Menelaou, M. J. P. Alcocer, T. Leijtens, L. M. Herz, A. Petrozza, H. J. Snaith, *Science* **2014**, *342*, 341.
[56] T. Du, W. Xu, S. Xu, S. R. Ratnasingham, C.-T. Lin, J. Kim, J. Briscoe, M. A. McLachlan, J. R. Durrant, *J. Mater. Chem. C* **2020**, *8*, 12648.
[57] J. Höcker, D. Kiermasch, P. Rieder, K. Tvingstedt, A. Baumann, V. Dyakonov, *Z. Naturforsch. A* **2019**, *74*, 665.
[58] K. W. Tsai, C. C. Chueh, S. T. Williams, T. C. Wen, A. K. Y. Jen, *J. Mater. Chem. A* **2015**, *3*, 9128.
[59] Z. Zhou, S. Pang, *J. Mater. Chem. A* **2020**, *8*, 503.
[60] W. Q. Wu, Q. Wang, Y. Fang, Y. Shao, S. Tang, Y. Deng, H. Lu, Y. Liu, T. Li, Z. Yang, A. Gruverman, J. Huang, *Nat. Commun.* **2018**, *9*, 1625.
[61] J. W. Lee, D. H. Kim, H. S. Kim, S. W. Seo, S. M. Cho, N. G. Park, *Adv. Energy Mater.* **2015**, *5*, 1501310.
[62] X. X. Gao, W. Luo, Y. Zhang, R. Hu, B. Zhang, A. Züttel, Y. Feng, M. K. Nazeeruddin, *Adv. Mater.* **2020**, *32*, 1905502.
[63] Z. Li, M. Yang, J. S. Park, S. H. Wei, J. J. Berry, K. Zhu, *Chem. Mater.* **2016**, *28*, 284.
[64] D. Y. Son, J. W. Lee, Y. J. Choi, I. H. Jang, S. Lee, P. J. Yoo, H. Shin, N. Ahn, M. Choi, D. Kim, N. G. Park, *Nat. Energy* **2016**, *1*, 16081.